

The ultraviolet photodissociation dynamics of IBr studied using state-selective translational spectroscopy

W. Sean McGivern, Runjun Li, Peng Zou, Trieu Nguyen, Simon W. North *

Department of Chemistry, Texas A&M University, P.O. Box 300012, College Station, TX 77842, USA

Received 8 July 1999

Abstract

We have investigated the ultraviolet photodissociation of IBr using core-sampled state-selective ion time-of-flight mass spectrometry on the iodine and bromine atom products. The branching ratios and anisotropy parameters were determined for the $I(^2P_{3/2}) + Br(^2P_{3/2})$, $I(^2P_{3/2}) + Br(^2P_{1/2})$, and $I(^2P_{1/2}) + Br(^2P_{3/2})$ channels at 248, 267, and 304 nm. We find no evidence for the $I(^2P_{1/2}) + Br(^2P_{1/2})$ channel at any wavelength. The results provide information on the relative transition probabilities for the $^3\Pi_1(2341)$, $^3\Pi_{0+}(2341)$, and $^1\Pi_1(2341)$ excited states in the absorption band centered at 270 nm. We have further evaluated the nonadiabatic curve crossing probability for the avoided crossing between the $^3\Pi_{0+}(2341)$ and $^3\Sigma_{0+}^-(2422)$ states over a range of wavelengths from 250 to 270 nm. The wavelength-dependent curve crossing probability for the avoided crossing is modeled using one-dimensional Landau–Zener theory in order to estimate the location of the avoided crossing and the splitting between adiabats. A comparison with recent work at 267 and 304 nm and analogous interhalogen molecules is also provided. © 1999 Elsevier Science B.V. All rights reserved.

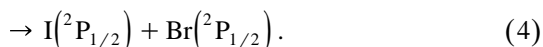
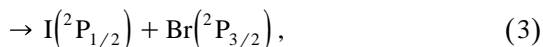
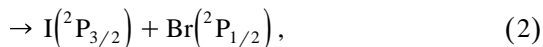
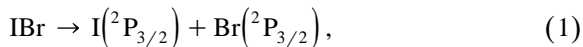
1. Introduction

The photodissociation of small molecules is an important area of research that has permitted significant insight into multiple electronic state dissociation dynamics, the nature and strength of potential couplings between states, and interference phenomena [1]. Diatomics are particularly well suited for studying these aspects of photoinitiated reactions and serve as benchmarks for our understanding of more complex systems. The electronic spectroscopy and photodissociation of heteronuclear and homonuclear diatomic halogens have a rich history as models for

characterizing subtle aspects of multistate dissociation. Recently, there has been a renewed experimental interest in these molecules using both photofragment imaging [2–7], in its various guises, and time-domain experiments. The absorption spectrum of IBr shows two broad peaks centered at 500 and 270 nm. The photodissociation of IBr in the visible region has been studied in great detail as an example of intermediate coupling between the diabatic (weak coupling) and adiabatic (strong coupling) limits [8–11]. The ground state of IBr has the configuration $(\sigma)^2(\pi)^4(\pi^*)^4(\sigma^*)^0$ and the term symbol $^1\Sigma_{0+}(2440)$, where the $(ijkl)$ suffix corresponds to an abbreviated notation for the configurations $(\sigma)^i(\pi)^j(\pi^*)^k(\sigma^*)^l$. Photodissociation at wavelengths near 270 nm, however, is less well characterized. In this wavelength region there are four ener-

* Corresponding author. E-mail: north@mail.chem.tamu.edu

getically allowed product channels, which include all combinations of ground state ($^2P_{3/2}$) and spin-orbit excited state ($^2P_{1/2}$) atoms (hereafter referred to as X and X*, respectively).



A schematic correlation diagram, restricted to excited states that are optically coupled to the ground state, is shown in Fig. 1. Diabatic correlations are shown as dashed lines and the adiabatic correlations, resulting from potential coupling, are shown as solid lines. The two lowest excited states corresponding to (2431) configurations are not involved in the initial photoexcitation at 260 nm but are important in the subsequent dissociation dynamics.

There have been two recent experimental studies of IBr photodissociation in the UV wavelength region. Jung et al. have studied the photodissociation

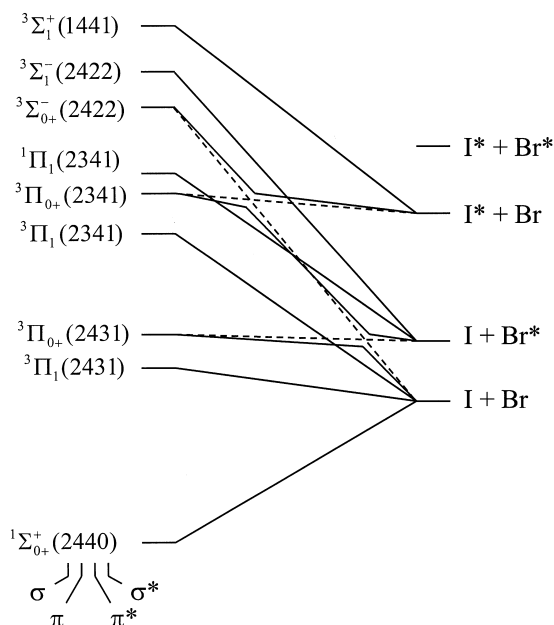


Fig. 1. Correlation diagram for the low-lying states of IBr. The diabatic correlations and adiabatic correlations are shown as dashed lines and solid lines, respectively.

of IBr at 304 nm using state-selective ion time-of-flight (TOF) spectroscopy [12]. They determined that the primary dissociation channel was I + Br, resulting from excitation to both the $^3\Pi_1(2341)$ and $^3\Pi_{0+}(2341)$ excited states. Very little of the $\text{I}^* + \text{Br}^*$ channel was observed. The $\text{I}^* + \text{Br}$ channel was thought to result from initial excitation to the $^3\Pi_{0+}(2341)$ state followed by nonadiabatic curve crossing to the $^3\Sigma_{0+}^-(2422)$ state, and the I + Br* channel was attributed to excitation to the $^1\Pi_1(2341)$ state followed by adiabatic dynamics. Based on the product channel branching ratios, the authors concluded that the transition to the $^3\Pi_1(2341)$ state dominated the oscillator strength at this wavelength. More recently, Kim et al., [13] using a center-stripe analysis of conventional photofragment images at 267 nm, observed a marked decrease in the I + Br channel compared to 304 nm and an increase in the parallel contribution to this channel. In addition, they reported an increase in the relative excitation probabilities for the higher energy $^1\Pi_1(2341)$ and $^3\Pi_{0+}(2341)$ states relative to the $^3\Pi_1(2341)$ state. The probability for the $^3\Sigma_{0+}^-(2422) \leftarrow ^3\Pi_{0+}(2341)$ nonadiabatic curve crossing was estimated as 0.69–1.00.

We have re-investigated the ultraviolet dissociation of IBr at 267 nm, probing both the bromine and iodine photofragments, which provides a greater confidence in the measured anisotropy parameters. Furthermore, we are able to precisely determine the branching ratios for all four energetically allowed channels without reliance on independent measurements to determine relative ionization probabilities. We have also extended measurements to other wavelengths, ranging from 304 to 248 nm to understand the nonadiabatic coupling between the $^3\Pi_{0+}(2341)$ and $^3\Sigma_{0+}^-(2422)$ excited states. At 267 nm, our results agree qualitatively with the work done by Kim et al., but we note some important differences. Most importantly, we find no significant decrease in the anisotropy parameter for the $\text{I}^* + \text{Br}$ channel from 304 to 267 nm and consequently find it unnecessary to identify an avoided crossing between the $^3\Sigma_{0+}^-(1411)$ and $^1\Pi_1(2341)$ states. Our results have also permitted a deconvolution of the ultraviolet absorption band into individual contributions from the $^1\Pi_1(2341)$, $^3\Pi_1(2341)$, and $^3\Pi_{0+}(2341)$ excited states.

2. Experimental

The time-of-flight apparatus has been described in detail elsewhere, and only the salient features and modifications to the previous set-up are reported here [14]. The instrument consists of a differentially pumped chamber with separate source and ionization regions. The molecular beam of 0.5% IBr in helium was generated by a solenoid pulsed valve (General Valve) with a 0.8 mm nozzle located ~ 7 cm from the interaction region. The beam was collimated with a 1.9 mm conical skimmer located 2 cm from the nozzle. Detection of the bromine and iodine photofragments was accomplished using 2 + 1 resonance-enhanced multiphoton ionization (REMPI) [15,16]. Laser pulses were generated by a pulsed dye laser (LAS) using Coumarin 500 (500–540 nm) or Rhodamine 640 (600–645 nm) pumped by the third harmonic (355 nm) or second harmonic (532 nm), respectively, of a Nd:YAG laser (Spectra-Physics) operating at 10 Hz. The dye laser fundamental was doubled in BBO, resulting in wavelengths of 250–270 or 300–322.5 nm. The doubled light was separated from the fundamental using two Pellin-Broca prisms and then passed through a double Fresnel rhomb and Glan-Taylor polarizer to allow precise alignment of the laser polarization. The light was focused into the interaction region with a $f = 300$ mm lens to a spot size of ~ 50 – 200 μm . For the 248 nm experiments, the output of a KrF excimer laser was counterpropagated with the dye laser probe beam and focused with a $f = 500$ mm lens. The laser power was monitored using a Molectron power meter as the light exited the chamber. Typical laser powers were 50–100 μJ /pulse for the dye laser and 2 mJ/pulse for the excimer laser.

A two-stage Wiley–McLaren time-of-flight mass spectrometer was used to detect the ionized photofragments [17]. The extraction region was typically held at ~ 20 V/cm, and the acceleration region at 245 V/cm. Two sets of deflector plates placed above the acceleration regions were used to translate the ion packet in the plane perpendicular to the detector axis. A copper plate with a 3.0 mm pinhole was placed ~ 29 cm from the interaction region, allowing only a ‘core’ of the ion packet to strike the detector. The ions were detected by a set of dual-chevron microchannel plates (Galileo) located

51 cm from the interaction region. The signal was averaged using a multi-channel scaler (Stanford Research Systems, SR430) with a 5 ns bin size.

The IBr (98%) sample was purchased from Aldrich and underwent several freeze–pump–thaw cycles to remove high vapor pressure contaminants prior to use.

3. Results and analysis

The velocity distribution of the photofragments along the detector axis, z , in the absence of core sampling is given by the following expression [18]:

$$I(v_z; \chi) = \int_{|v_z|}^{\infty} \frac{g(v)}{2v} \left[1 + \beta P_2(\cos \chi) P_2\left(\frac{v_z}{v}\right) \right] dv, \quad (5)$$

where β is the spatial anisotropy parameter, $P_2(x)$ is the second Legendre polynomial, $g(v)$ is the distribution of speeds, and $\cos \chi = \hat{\epsilon} \cdot \hat{z}$ is the projection of the laser electric field on the detector axis. Core sampling selects only those fragments with small velocity projections perpendicular to the detector axis, and under these conditions Eq. (5) is modified to include only speeds in the range v_z^{\min} to v_z^{\max} where

$$v_z^{\max} = v, \\ v_z^{\min} = \sqrt{v^2 - v_{\text{core}}^2}, \quad (6)$$

and v_{core} is the maximum speed not discriminated by the coring aperture [19–21]. In general, either the forward convolution method or direct inversion can be employed to determine the speed distribution. However, for a diatomic molecule the partitioning of the available energy is trivial, involving only electronic excitation of the photofragments. The total translational energy, E_T , is thus given by

$$E_T = E_{h\nu} - D_0^0(\text{I-Br}) - E_{\text{SO}} + E_{v,J}^{\text{parent}}, \quad (7)$$

where $E_{h\nu}$ is the energy of the dissociation photon, $D_0^0(\text{I-Br})$ is the bond dissociation energy of IBr, E_{SO} is the total spin–orbit energy of the iodine and/or

bromine atoms, and $E_{v,J}^{\text{parent}}$ is the internal energy of the parent molecule prior to dissociation. Spectroscopic studies using 2 + 1 REMPI of jet-cooled IBr have demonstrated rotational temperatures of 15 K and vibrational temperatures of 300 K from a heated nozzle under comparable expansion conditions to those of this study [22] and therefore, we neglect the internal energy of the parent ($< 300 \text{ cm}^{-1}$). Using Eq. (7), we can precisely determine the velocity of each fragment for a given photon energy and dissociation channel. The experimental velocities are derived from TOF spectra by transforming to velocity space using the linear relation, $v_z = qV_{\text{ex}} t/m$, where q is the charge of the fragment ion, m is the mass of the fragment, t is the time offset from the center of the profile, and V_{ex} is the strength of the electric field in the extraction region [21]. We find that the measured velocities correspond to within $\pm 10 \text{ m/s}$ of the theoretical values. Further analysis of the TOF spectra only requires that the channels be sufficiently resolved to permit unambiguous integration.

Representative TOF spectra are shown in Figs. 2 and 3 for the bromine and iodine products, respectively, from IBr photodissociation near 267 nm. There are several factors that produce the finite width of each TOF peak. The first is the finite size of the core, which results in different values of v_z^{max} and v_z^{min} and is a minor effect in the present case, contributing 10 ns to the width. The laser pulse length, represented by a Gaussian with a FWHM of 10 ns, also broadens the peaks. Finally, the tail which extends toward slower velocities for each peak is due to the finite ionization volume from the focused laser, which results in a superposition of ion packets which are displaced relative to the center of the pinhole. Forward convolution simulations quantitatively reproduce the experimental observations, and the broadening effects do not significantly alter the analysis described below. The Br spectrum, shown in the top panel of Fig. 2, shows two sets of four peaks. The four peaks are due to the formation of coincident I and I*, and each set corresponds to a given isotope of bromine, ^{79}Br and ^{81}Br . The outer set of peaks corresponds to the I + Br channel, and the inner set of peaks corresponds to I* + Br. The TOF spectrum of Br*, shown in the lower panel of Fig. 2, corresponds to a single channel, I + Br*. No I* + Br* signal was observed. Similar data are shown in

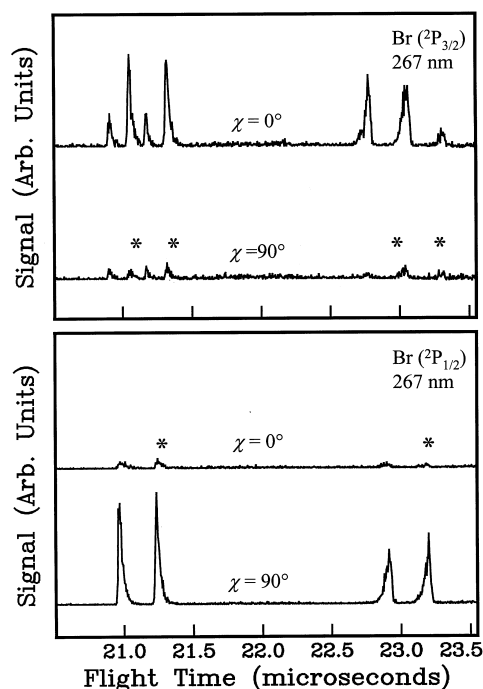


Fig. 2. Core-sampled time-of-flight spectra for Br (top panel) and Br* (bottom panel) arising from IBr photodissociation near 267 nm. The asterisks indicate the peaks corresponding to the ^{81}Br isotopes. The angle between the electric field vector of the dissociation laser and the flight axis, χ , is indicated.

Fig. 3 for the detection of I and I*, which corresponds to a single isotope, ^{127}I .

The anisotropy parameter, β , is given by:

$$\beta = \frac{I(\chi = 0^\circ) - I(\chi = 90^\circ)}{\frac{1}{2}I(\chi = 0^\circ) + I(\chi = 90^\circ)}, \quad (8)$$

where $I(\chi)$ are the intensities of the TOF peaks for the parallel ($\chi = 0^\circ$) and perpendicular ($\chi = 90^\circ$) detection geometries. The application of Eq. (8) using point-by-point differences has been used previously to measure velocity-dependent anisotropy parameters [12,19,23]. This procedure is extremely noisy and can lead to an apparent velocity dependence of the anisotropy parameter even for a single speed, which is especially strong at low values of v_z . However, *integration* of the individual peaks allows a direct determination of the anisotropy parameter, provided a correction for the finite coring aperture is applied. Substitution of a finite integral of Eq. (5) from v_z^{min} to v_z^{max} for a single speed into Eq. (8)

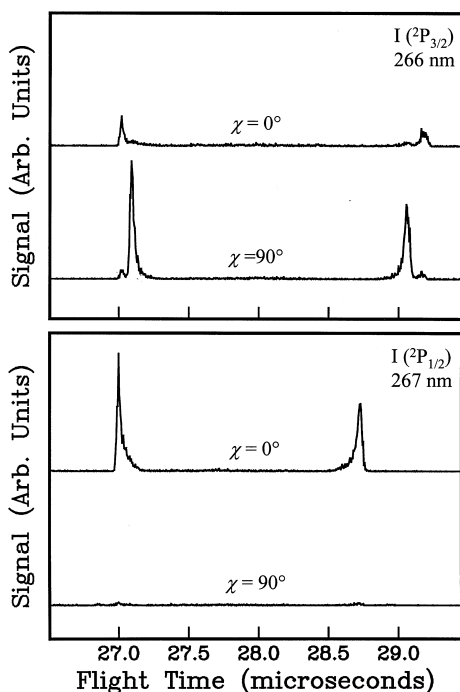


Fig. 3. Core-sampled time-of-flight spectra for I (top panel) and I^* (bottom panel) arising from IBr photodissociation near 267 nm. The angle between the electric field vector of the dissociation laser and the flight axis, χ , is indicated.

yields a correction factor for the finite core size. The corrected anisotropy parameter, β_{corr} , is then

$$\beta_{\text{corr}} = \beta_{\text{uncorr}} \left(\frac{2}{s + s^2} \right), \quad (9)$$

where

$$s = \frac{\sqrt{v^2 - v_{\text{core}}^2}}{v} \quad (10)$$

is the correction for a finite core size and β_{uncorr} is the anisotropy parameter determined by using integrated peak intensities in Eq. (8). In the limit of an infinitesimally small core, ζ reduces to 1.0. A significant advantage to probing *both fragments* from each dissociation channel is that it provides a consistency check on the determined anisotropy parameter and a measure of alignment effects. We find that the observed anisotropy parameters obtained for each channel are internally consistent to within the stated error bars except for the $I^* + \text{Br}$ channel. The anisotropy parameter for the I^* atom from this channel is 1.90

at 267 nm while the anisotropy parameter measured for the Br atom was ~ 1.4 , similar to the results of Kim et al. Alignment of atomic angular momentum from diatomic photodissociation has been reported previously [6,24–26]. In the presence of product alignment, the β parameter in Eq. (5) is a function of both the spatial anisotropy parameter and the laboratory-frame quadrupole alignment. Although no atomic alignment is possible when the angular momentum is $J = 1/2$ as in $I^*(^2P_{1/2})$, there can be alignment of the $\text{Br}(^2P_{3/2})$ atom, particularly in the case of excitation to an $\Omega = 0^+$ state (vide infra) which possesses no net angular momentum projection on the internuclear axis. Conservation of angular momentum requires that the Br atoms can populate only $m_J = \pm 1/2$, resulting in less than limiting values of β [25]. We, therefore, assign the anisotropy parameters for this channel based on the I^* results for all wavelengths studied.

The determination of the branching ratios requires adding the vertical ($\chi = 0^\circ$) TOF and horizontal ($\chi = 90^\circ$) TOF spectra in a 1:2 ratio to remove the spatial anisotropy. The ratio of the integrated peak intensities for each channel in these coadded spectra determines the relative branching ratio between channels that contained the detected photofragment after the ratio of the integrated peak intensities is scaled by a velocity factor:

$$\frac{N(X^*)}{N(X)} = \frac{I(X^*)}{I(X)} \frac{v_{X^*}}{v_X}, \quad (11)$$

where $X = \text{Br}$ or I is the counterfragment to the detected atom. The application of Eq. (11) to all of the spectra taken near 267 nm results in a system of equations describing the branching ratio between each of the possible dissociation channels. Since the $2 + 1$ REMPI lines used for detection were in very close spectral proximity no correction for the IBr absorption cross-section was necessary. Solving this system of equations and normalizing the result, we find the overall branching ratio for each channel. This method is inherently more sensitive than the determination of branching ratios by correcting for the difference in ionization cross-sections based on a calibration compounds. We have also determined anisotropy parameters and branching ratios at 248 and 304 nm. The 304 nm branching ratios were

Table 1

Anisotropy parameters and product branching ratios for IBr photodissociation at 248, 267, and 304 nm

Dissociation channel	248 nm		267 nm		304 nm		304 nm ^a	
	branching ratio	β	branching ratio	β	branching ratio	β	branching ratio	β
$I(^2P_{3/2}) + Br(^2P_{3/2})$	< 0.01	1.90	0.13 ± 0.03	0.94 ± 0.1	0.67 ± 0.03	-0.05	0.61	0.0
$I(^2P_{3/2}) + Br(^2P_{1/2})$	0.83 ± 0.06	-0.97	0.60 ± 0.03	-0.85 ± 0.1	0.26 ± 0.03	-0.64	0.29	-0.7
$I(^2P_{1/2}) + Br(^2P_{3/2})$	0.16 ± 0.06	2.00	0.27 ± 0.03	1.90 ± 0.2	0.07 ± 0.03	2.00	0.10	1.8
$I(^2P_{1/2}) + Br(^2P_{1/2})$	0.00		0.00		0.00		< 0.01	

^aData from Ref. [12].

determined using the ratio of ionization probabilities, $[I^*]/[I] = 0.769$, reported by Jung et al. [12] Table 1 gives the branching ratios and anisotropy parameters for the four possible channels at each wavelength. Also shown in Table 1 are the results from the previous study performed by Jung et al. at 304 nm. We have reanalyzed the branching ratios from the results of the previous study to correctly quantify the parallel and perpendicular contributions to each

channel. We find that the observed branching ratios and anisotropy parameters at 304 nm are consistent with the results of Jung et al. We note, however, some important differences between our results and the recent results of Kim et al. at 267 nm [13]. We find a more negative anisotropy parameter for the $I + Br^*$ channel (-0.85 vs. -0.75), which indicates a near-limiting perpendicular transition. In addition, the anisotropy parameter at 267 nm observed in this study for the $I^* + Br$ channel is 1.90, indicating a strongly parallel transition and which is significantly higher than the 1.30 determined by Kim et al.

To examine the wavelength dependence of the anisotropy parameter for each product channel, TOF spectra were taken at several other $2 + 1$ REMPI transitions. Br^* was probed at 262.5 nm, and Br was probed at 250.3, 250.9, and 260.6 nm. TOF spectra for Br at 260.6 nm and Br^* at 262.5 nm are shown in Fig. 4. Table 2 lists the anisotropy parameters and product channel branching ratios for each wavelength. For all three observed channels, the anisotro-

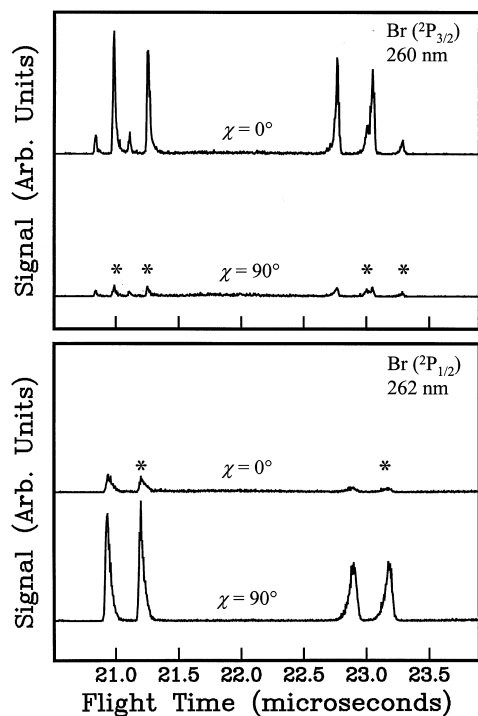


Fig. 4. Core-sampled time-of-flight spectra for Br at 260 nm (top panel) and Br^* at 262 nm (bottom panel) arising from IBr photodissociation. The asterisks indicate the peaks corresponding to the ^{81}Br isotopes. The angle between the electric field vector of the dissociation laser and the flight axis, χ , is indicated.

Table 2

Anisotropy parameters and product branching ratios for IBr photodissociation probed using $2 + 1$ REMPI on the Br or Br^* products

Channel	Wavelength (nm)	β	Branching ratio
$I + Br$	250.3	2.0 ± 0.1	0.05 ± 0.04
$I^* + Br$		1.9 ± 0.1	0.95 ± 0.04
$I + Br$	250.9	2.0 ± 0.1	0.17 ± 0.04
$I^* + Br$		2.0 ± 0.1	0.83 ± 0.04
$I + Br$	260.6	0.86 ± 0.1	0.19 ± 0.04
$I^* + Br$		1.9 ± 0.1	0.81 ± 0.04
$I + Br^*$	262.5	-0.74 ± 0.1	1.0
$I^* + Br^*$			0.0

py parameters become more limiting with decreasing wavelength. No evidence for the $I^* + Br^*$ channel was observed for any of the wavelengths studied.

4. Discussion

4.1. Transition probabilities

The branching ratios and anisotropy parameters for each channel provide a means to determine the individual transition probabilities for the ${}^3\Pi_{0+}$ (2341), ${}^1\Pi_1$ (2341), and ${}^3\Pi_1$ (2341) excited states. We believe that excitation occurs to only these states in the Franck–Condon region. States in the (2431) band are expected to contribute to absorption near 500 nm and will not play a role in the ultraviolet absorption band [9]. Furthermore, the transition dipole moment is expected to be extremely small for two-electron excitation, decreasing the possibility for absorption to states in the (2422) band and above. The term symbols for IBr according to spin–orbit coupling are characterized by Ω , the projection of the total angular momentum along the internuclear axis. A parallel transition occurs when $\Delta\Omega = 0$, and a perpendicular transition occurs when $\Delta\Omega = \pm 1$. Dissociation from a parallel transition results in an angular distribution described by an anisotropy parameter of 2.0, and dissociation from a perpendicular state results in an anisotropy parameter of -1.0 . Since the ground state of IBr is $\Omega = 0$, transitions to the ${}^3\Pi_{0+}$ (2341) state are parallel, and transitions to the ${}^3\Pi_1$ (2341) and ${}^1\Pi_1$ (2341) states are perpendicular. Since coherent effects influence only the rotational polarization and not the velocity anisotropy [27,28], the observed anisotropy parameter, β_{obs} , may be considered a linear combination of the limiting values for parallel ($\beta_{\parallel}^{\text{lim}} = 2.0$) and perpendicular ($\beta_{\perp}^{\text{lim}} = -1.0$) transitions:

$$\beta_{\text{obs}} = a_{\parallel} \beta_{\parallel}^{\text{lim}} + a_{\perp} \beta_{\perp}^{\text{lim}}. \quad (12)$$

The coefficients a_{\parallel} and a_{\perp} of this linear combination give the relative contribution of states corresponding to parallel and perpendicular symmetries, respectively. With the fraction of parallel and perpendicular character for each state known, the total transition probabilities for each state can be determined.

Both the ${}^1\Pi_1$ (2341) and ${}^3\Pi_{0+}$ (2341) states lead adiabatically to $I + Br^*$ products. The ${}^3\Pi_{0+}$ (2341) state forms two avoided crossings with additional 0^+ curves. The first avoided crossing involves the high-lying ${}^3\Sigma_{0+}^-$ (2422) state and the second involves the lower ${}^3\Pi_{0+}$ (2431) state. Since only the ${}^1\Pi_1$ (2341) and ${}^3\Pi_{0+}$ (2341) states correlate to $I + Br^*$ products in this wavelength region, the observation of this channel must be a result of adiabatic dynamics in the dissociation. The measured anisotropy parameter for the $I + Br^*$ channel at 267 nm is -0.85 ± 0.1 , corresponding to a strongly perpendicular transition (0.95). The branching ratio for the $I + Br^*$ channel is 0.60 ± 0.03 and, therefore, the probability of excitation to the ${}^3\Pi_{0+}$ (2341) state followed by adiabatic dissociation to give $I + Br^*$ is 0.03. The ${}^3\Pi_{0+}$ (2341) state can also yield the $I^* + Br$ and $I + Br$ product channels via nonadiabatic curve crossing. The total transition probability for the ${}^3\Pi_{0+}$ (2341) state is determined by the sum of the parallel contributions to these additional channels. The total transition probabilities for the other states are obtained in a similar fashion. Table 3 shows the derived transition probability for each excited state at 248, 267, and 304 nm.

4.2. Nonadiabatic dynamics

The two well-documented avoided crossings in IBr dissociation are shown in Fig. 1. The lower crossing, ${}^3\Pi_{0+}$ (2430) \leftarrow ${}^3\Sigma_{0+}^-$ (2422), has been the subject of considerable study but has only modest influence on the dynamics at these wavelengths. Child has studied the dynamics of IBr dissociation for excitation energies near the lower avoided crossing using a one-dimensional Landau–Zener analysis [9]. The author calculated a splitting between adiabats, $V_{12} = 170 \text{ cm}^{-1}$, and the location of the avoided

Table 3
Excited state transition probabilities for IBr using the data in Table 1 (see text for details)

Excited state	248 nm	266 nm	304 nm	304 nm ^a
${}^3\Pi_{0+}$ (2341)	0.19 ± 0.08	0.38 ± 0.04	0.32 ± 0.04	0.33
${}^1\Pi_1$ (2341)	0.81 ± 0.08	0.57 ± 0.05	0.22 ± 0.04	0.26
${}^3\Pi_1$ (2341)	0.00 ± 0.08	0.05 ± 0.04	0.46 ± 0.04	0.41

^aData from Ref. [12].

crossing, $E = 16915 \text{ cm}^{-1}$ at 3.220 \AA . Adopting the parameters of Child at the available energies relevant to this study, we find that the nonadiabatic transition probability is near unity and, therefore, have assumed that the dissociation proceeds diabatically through this lower avoided crossing. The avoided crossing between the $^3\Pi_{0+}(2341)$ and $^3\Sigma_{0+}^-(2422)$ excited states is less well studied and plays a prominent role in the dissociation at shorter wavelengths. Recently, Tonokura et al. [3] calculated the splitting between these adiabatic curves in ICl as $V_{12} = 294 \text{ cm}^{-1}$. Though the magnitudes of the splittings differ for the lower avoided crossing between ICl and IBr [10], the difference is not large, and a comparable difference would be expected for the upper crossing.

Since we do not consider excitation to the $^3\Sigma_{0+}^-(2422)$ state to be important, the observation of a near-limiting parallel anisotropy parameter associated with the $I^* + \text{Br}$ channel requires that these products arise from a nonadiabatic curve crossing. Adiabatically, the $^3\Pi_{0+}(2341)$ state correlates to $I + \text{Br}^*$. However, the $^3\Pi_{0+}(2431) \leftarrow ^3\Sigma_{0+}^-(2422)$ avoided crossing allows essentially complete curve crossing at the wavelengths in this study. Therefore, trajectories which remain on the lower adiabat through the higher-energy crossing will give $I + \text{Br}$ products. The only possible parallel contribution to the $I + \text{Br}$ and $I^* + \text{Br}$ channels is from the $^3\Pi_{0+}(2341)$ state. Therefore, a measure of the relative parallel contributions to the $I^* + \text{Br}$ and $I + \text{Br}$ channels provides a direct measure of the nonadiabatic curve crossing probability. Using this analysis, the crossing probability can then be determined at wavelengths down to 250 nm for any $\text{Br } 2 + 1$ REMPI transition. Other formulations exist to determine the nonadiabatic crossing probability using the relative branching ratio and relative excitation probabilities when absorption occurs to both states [5,13]. However, we neglect excitation to the $^3\Sigma_{0+}^-(2422)$ excited state, so the more direct method described above may be used to determine the crossing probability.

An additional avoided crossing between $\Omega = 1$ states, $^3\Sigma_1^+(1411) \leftarrow ^1\Pi_1(2341)$, has been suggested by Kim et al. which allows the $^1\Pi_1(2341)$ state to make a perpendicular contribution to the $I^* + \text{Br}$ channel. The presence of this crossing was invoked to explain the observed decrease in the anisotropy

parameter of the $I^* + \text{Br}$ channel when the excitation energy was increased from 304 to 266 nm . However, we observe no significant change in the anisotropy parameter for this channel between 304 and 266 nm . Furthermore, the presence of this crossing would result in larger perpendicular contributions at shorter excitation wavelengths because the nonadiabatic crossing probability should increase with increasing radial velocity. Since we observe near-limiting parallel anisotropy parameters for this channel at wavelengths down to 250 nm , we do not find compelling evidence for this avoided crossing.

Nonadiabatic curve crossing probabilities may be estimated using one-dimensional Landau–Zener theory. The probability, P , of a nonadiabatic curve crossing is given by

$$P = \exp\left(-\frac{2\pi V_{12}^2}{\hbar v |\Delta F|}\right), \quad (13)$$

where $2 \cdot V_{12}$ is the splitting between adiabats at the avoided crossing, v is the radial velocity of the photofragments at the crossing point, and $|\Delta F|$ is the difference in slopes. The curve crossing probability as a function of wavelength is shown in Fig. 5. A clear increase in the probability of nonadiabatic curve crossing with decreasing wavelength is observed, ranging from 0.24 at 304 nm to 0.92 at 250 nm .

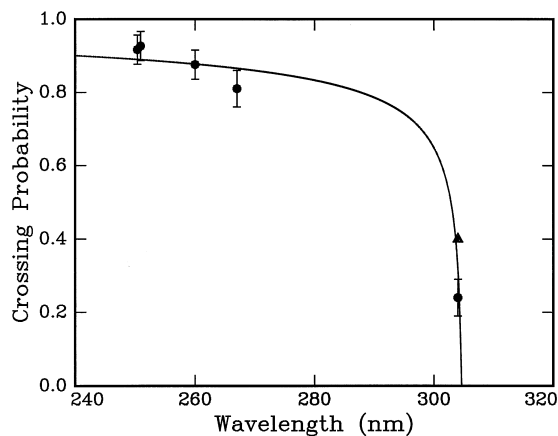


Fig. 5. Nonadiabatic curve crossing probability as a function of wavelength for the $^3\Sigma_{0+}^-(2422) \leftarrow ^3\Pi_{0+}(2341)$ transition. The circles represent the crossing probabilities determined in this study, and the triangle is the crossing probability evaluated from the results of Ref. [12]. The solid line is a best fit to the experimental data.

Using Eq. (12), the wavelength dependence of the crossing probability can be modeled in order to extract both the energy of the crossing point, which determines the radial velocity, and a factor, $c = 2\pi V_{12}^2/\hbar|\Delta F|$. The energy of the avoided crossing using this analysis is $32\,830\text{ cm}^{-1}$, and the factor $c = 52\text{ m/s}$. We find that this value of c is consistent to estimates determined by using the reported splittings of similar adiabats [8,9]. The energy of the avoided crossing is very close to the energy from 304 nm excitation, which is consistent with the small nonadiabatic crossing probability observed at this wavelength and the dramatic increase in the probability with wavelengths decreasing from 304 nm. Even at wavelengths as long as 267 nm, the nonadiabatic curve crossing probability is greater than 0.90 for this avoided crossing. Therefore, for wavelengths shorter than 267 nm, only a small ground state product channel would be expected.

4.3. Nature of the UV band

For purely repulsive potentials and an initial Gaussian wavepacket in the ground electronic state, the absorption band for a specific excited state may be approximated by a Gaussian function [29]. The width of the Gaussian is related to the slope of the electronic potential energy surface in the Franck–Condon region, and the center of the peak may be taken to first order as the vertical excitation energy. The reported ultraviolet absorption spectrum [30] for

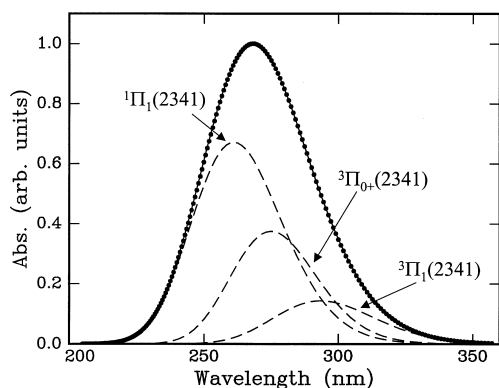


Fig. 6. Decomposition of the literature absorption spectrum (Ref. [30]) of IBr into contributions from transitions to the $^3\Pi_1(2341)$, $^3\Pi_{0+}(2341)$, and $^1\Pi_1(2341)$ excited states.

Table 4

Gaussian parameters for the decomposition of the UV absorption spectrum based on the model presented in the text

	$^1\Pi_1(2341)$	$^3\Pi_0(2341)$	$^3\Pi_1(2341)$
N_i	0.670	0.374	0.143
E_i (cm^{-1})	38306	36369	34069
ξ_i (cm^{-1})	3470.0	2943.1	3055.6
Slope in FC region ($\text{cm}^{-1}\text{ \AA}^{-1}$)	48553	41241	42755

IBr was fitted by three Gaussian functions of the form

$$\sigma(E) = \sum_{i=1}^3 A_i \exp\left[-\left(\frac{E - E_i}{\xi_i}\right)^2\right] \quad (14)$$

corresponding to the $^3\Pi_1(2341)$, $^3\Pi_{0+}(2341)$, and $^1\Pi_1(2341)$ excited states. The fit was additionally constrained to reproduce the relative transition probabilities at 248, 267, and 304 nm determined in the present experiment. Based on the one-dimensional reflection principle [29], an estimate of the slope of the potential energy surface in the Franck–Condon region may be obtained from the ratio of the full width at half maximum (FWHM) of the Gaussian absorption spectrum to the FWHM of the ground vibrational state probability distribution (0.12 \AA^{-1}). The resulting decomposition of the UV absorption band is shown in Fig. 6, and the Gaussian parameters are listed in Table 4, along with vertical excitation probabilities and the slopes of the potential energy surfaces. Contributions from all three optically allowed excited states in the (2341) band are significant in the absorption spectrum. To our knowledge, this represents the first complete decomposition of the ultraviolet absorption spectrum for interhalogen diatomic molecules reported in the literature.

4.4. Comparison to other interhalogen diatomic molecules

The ultraviolet dynamics of interhalogen diatomic molecules has recently been the focus of experimen-

¹ The effect of hot-bands has been neglected in our treatment. However, we note that at 300 K the fraction of molecules in the vibrational ground state is 0.72 and that this approximation is not severe.

tal and theoretical investigation. Despite this attention, there remain conflicting opinions as to the nature of the absorption band. Several studies have assigned the UV band exclusively to a $\Omega = 0^+$ state [31–33], although the observation of non-limiting parallel anisotropy suggests that a $\Omega = 1$ state is also involved. In BrCl, Cooper et al. [5] have assigned the parallel component to the $^3\Sigma_{0+}^-$ (2422) excited state and the perpendicular component to the $^3\Sigma_{1-}^-$ (2422) state. However, in ICl, the perpendicular component has been assigned to the $^1\Pi_1$ (2341) state [3], and the parallel component both to the $^3\Pi_{0+}$ (2341) state [3] and the $^3\Sigma_{0+}^-$ (2422) state [2]. In the present study we suggest that the $^3\Pi_{0+}$ (2341) and $^1\Pi_1$ (2341) states make the major contributions to the UV spectrum of IBr. Given the apparent similarity between these molecules, such dramatic differences would be unexpected. In order to characterize the ultraviolet absorption spectrum of each molecule fully, a quantitative, wavelength-dependent determination of the anisotropy parameters and product branching ratios must be performed. However, the deconvolution of the UV absorption band of IBr (Fig. 6) may provide insight into the nature of the electronic excited states of other diatomic halogens.

Recent experiments have shown that both ICl and BrCl exhibit similar dissociation dynamics to IBr. Initially, ICl was believed to dissociate through three channels in the ultraviolet region, $I + Cl$, $I + Cl^*$, and $I^* + Cl$ [3]. Tonokura et al. calculated the relative transition probabilities for the electronic excited states in the ultraviolet band and found that excitation primarily occurred to the $^3\Pi_{0+}$ (2341) and $^1\Pi_1$ (2341) states. The calculations revealed a small contribution from the $^3\Sigma_{0+}^-$ (2422) state, but the oscillator strength was much smaller than for the one-electron excitations. Since the nonadiabatic transition probability between the $^3\Sigma_{0+}^-$ (2422) and $^3\Pi_{0+}$ (2341) states is near unity, excitation to the $^3\Pi_{0+}$ (2341) state would be expected to give ground state products, provided the trajectory followed an adiabatic path through the upper avoided crossing. However, subsequent ion imaging experiments by Rogers et al. [2] found no evidence for the $I + Cl$ channel. As a result, the parallel component of the $I^* + Cl$ channel was assigned to the state. In IBr, the nonadiabatic transition probability at the upper crossing increases quickly at increasing excitation energies (Fig. 5).

The calculations by Tonokura et al. on ICl find a splitting between adiabats of only 292 cm^{-1} . Since the splitting would not be expected to be largely different for IBr, a similar increase in the crossing probability for decreasing wavelengths would be expected in ICl depending on the location of the crossing point. Therefore, excitation to the $^3\Pi_{0+}$ (2341) state of ICl could result in a strongly parallel anisotropy parameter for the $I^* + Cl$ channel and only a minor yield of the ground state product channel. This observation would be consistent with the experimental results of Rogers et al. and the calculations of Tonokura et al., which show preferential excitation to the $^3\Pi_{0+}$ (2341).

The UV photodissociation of BrCl is similar to IBr and ICl and results in only two channels, $Br + Cl^*$ and $Br^* + Cl$ [5]. The parallel excitation leading to the $Br^* + Cl$ channel was assigned to the $^3\Sigma_{0-}^-$ (2422) state, and the perpendicular excitation leading to the $Br + Cl^*$ channel was attributed to the $^3\Sigma_{1-}^-$ (2422) state. As in ICl, excitation to the $^3\Pi_{0+}$ (2341) state was discounted because the $Br + Cl$ channel was not observed. However, if excitation occurs to the $^3\Pi_{0+}$ (2341) state, a sharp increase in the nonadiabatic crossing probability with increasing excitation energy would also result in the lack of a ground state product channel for the wavelengths used by Cooper et al. Furthermore, excitation to a two-electron state, considered a minor contribution to the UV band in ICl, is not required. The assignment of the perpendicular component of the absorption spectrum to the $^3\Sigma_{1-}^-$ (2422) state is not absolute, since excitation to the $^1\Pi_1$ (2341) state is consistent with the observation of the $Br + Cl^*$ channel. The assignment of the perpendicular component to the $^1\Pi_1$ (2341) also appears more reasonable because the expected transition probability for a one-electron transition is expected to be substantially higher than for a two-electron transition. Furthermore, the $^1\Pi_1$ (2341) state is assigned as the major perpendicular contribution to the absorption spectrum in both IBr and ICl. Therefore, ultraviolet excitation would be expected to occur primarily to the $^3\Pi_{0+}$ (2341) and $^1\Pi_1$ (2341) excited states of BrCl.

The photodissociation dynamics of BrCl and ICl show a remarkable similarity to those of IBr. Although the absorption spectra of both BrCl and ICl are now known to consist of both parallel and per-

pendicular components, the assignment of these transitions continues to be subject of conflicting reports. Our decomposition of the absorption spectrum of IBr into individual excited state components based on the wavelength appears to be consistent with previous experimental observations other diatomic interhalogens. We believe that the UV absorption spectra of both BrCl and ICl may consist primarily of $^1\Pi_1(2341)$ and $^3\Pi_{0+}(2341)$ components with a minor contribution from the $^3\Pi_1(2341)$ state in analogy IBr.

5. Summary

The ultraviolet photodissociation of IBr has been examined using resonance enhanced multiphoton ionization (REMPI) with core-sampled time-of-flight mass spectrometry at wavelengths ranging from 248 to 304 nm. Anisotropy parameters, product branching ratios, and relative transition probabilities have been determined at 248, 267, and 304 nm. Furthermore, nonadiabatic curve crossing probabilities have been determined for several wavelengths between 250 and 270 nm. The location of the avoided crossing was also estimated by modeling the wavelength dependence of the nonadiabatic curve crossing probability using Landau–Zener theory. We find that the dissociation dynamics become increasingly nonadiabatic at shorter wavelengths. The ultraviolet absorption spectrum for IBr has also been decomposed into three components, corresponding to the $^3\Pi_{0+}(2341)$, $^1\Pi_1(2341)$, and $^3\Pi_1(2341)$ excited states. The proposed decomposition is consistent with the current literature for ICl and BrCl, and the absorption spectra of these molecules probably consist of large $^3\Pi_{0+}(2341)$ and $^1\Pi_1(2341)$ contributions with a minor contribution from the $^3\Pi_1(2341)$ state. Further measurements on the wavelength-dependent anisotropy and branching ratios are necessary to confirm this correspondence.

Acknowledgements

The authors would like to thank Dr. Robert R. Lucchese and Dr. Michael B. Hall for their helpful

comments. This work was supported by the Texas Research Endowment Fund.

References

- [1] R. Schinke, *Photodissociation Dynamics*, Cambridge University Press, Cambridge, 1993.
- [2] L.J. Rogers, M.N.R. Ashfold, Y. Matsumi, M. Kawasaki, B.J. Whitaker, *Chem. Phys. Lett.* 258 (1996) 159.
- [3] K. Tonokura, Y. Matsumi, M. Kawasaki, H.L. Kim, S. Yabushita, S. Fujimura, K. Santo, *J. Chem. Phys.* 99 (1993) 3461.
- [4] T.P. Rakitzis, S.A. Kandel, A.J. Alexander, Z.H. Kim, R.N. Zare, *Science* 281 (1998) 1346.
- [5] M.J. Cooper, P.J. Jackson, L.J. Rogers, A.J. Orr-Ewing, M.N.R. Ashfold, B.J. Whitaker, *J. Chem. Phys.* 109 (1998) 4367.
- [6] A.S. Bracker, E.R. Wouters, A.G. Suits, Y.T. Lee, O.S. Vasuyutinskii, *Phys. Rev. Lett.* 80 (1998) 1626.
- [7] P.C. Samartzis, I. Sakellariou, T. Gougousi, T.N. Kitsopolous, *J. Chem. Phys.* 107 (1997) 43.
- [8] M. Shapiro, M.J.J. Vrakking, A. Stolow, *J. Chem. Phys.* 110 (1999) 2465.
- [9] M.S. Child, *Mol. Phys.* 32 (1976) 1495.
- [10] M.S. Child, R.B. Bernstein, *J. Chem. Phys.* 59 (1973) 5916.
- [11] M.B. Faist, R.B. Bernstein, *J. Chem. Phys.* 64 (1976) 2971.
- [12] K. Jung, J.A. Griffiths, M.A. El-Sayed, *J. Chem. Phys.* 103 (1995) 6999.
- [13] Y.S. Kim, Y.J. Jung, K.H. Jung, *J. Chem. Phys.* 107 (1997) 3805.
- [14] W.S. McGivern, R. Li, P. Zou, S.W. North, *J. Chem. Phys.* 111 (1999) 5771.
- [15] S. Arepalli, N. Presser, D. Robie, R.J. Gordon, *Chem. Phys. Lett.* 117 (1985) 64.
- [16] K. Bergmann, R.T. Carter, G.E. Hall, J.R. Huber, *J. Chem. Phys.* 109 (1998) 474.
- [17] W.C. Wiley, I.H. McLaren, *Rev. Sci. Instrum.* 26 (1955) 1150.
- [18] R.N. Zare, *Mol. Photochem.* 4 (1972) 1.
- [19] H.J. Hwang, J. Griffiths, M.A. El-Sayed, *Int. J. Mass Spectrom. Ion Processes* 131 (1994) 265.
- [20] R. Ogorzalek-Loo, H.-P. Haerri, G.E. Hall, P.L. Houston, *J. Chem. Phys.* 90 (1989) 4222.
- [21] J.A. Syage, *J. Chem. Phys.* 105 (1996) 1007.
- [22] A.J. Yencha, T. Ridley, R. Maier, R.V. Flood, K.P. Lawley, R.J. Donovan, A. Hopkirk, *J. Phys. Chem.* 97 (1993) 4582.
- [23] J.A. Griffiths, K.W. Jung, M.A. El-Sayed, *J. Phys. Chem.* 100 (1996) 7989.
- [24] Y. Yang, H.P. Loock, J. Cao, C.X.W. Qian, *J. Chem. Phys.* 102 (1995) 808.
- [25] P.C. Samartzis, B.L.G. Bakker, T.P. Rakitzis, D.H. Parker, T.N. Kitsopoulos, *J. Chem. Phys.* 110 (1999) 5201.
- [26] T.P. Rakitzis, S.A. Kandel, A.J. Alexander, Z.H. Kim, R.N. Zare, *J. Chem. Phys.* 110 (1999) 3351.

- [27] L.D.A. Siebbeles, M. Glass-Maujean, O.S. Vasyutinskii, J.A. Beswick, O. Roncero, *J. Chem. Phys.* 100 (1994) 3610.
- [28] D.V. Kupriyanov, O.S. Vasyutinskii, *Chem. Phys.* 171 (1993) 25.
- [29] E.U. Condon, *Phys. Rev.* 32 (1928) 858.
- [30] D.J. Seery, D. Britton, *J. Phys. Chem.* 68 (1964) 2263.
- [31] S. Hubinger, J.B. Nee, *J. Photochem. Photobiol. A* 86 (1995) 1.
- [32] K. Balsubramanian, *J. Mol. Spectrosc.* 110 (1985) 339.
- [33] K. Balsubramanian, *Chem. Phys.* 95 (1985) 225.